Biochemistry **2004,** *43,* 13271−13282

Orientation of Calcium in the Mn_4Ca Cluster of the Oxygen-Evolving Complex Determined Using Polarized Strontium EXAFS of Photosystem II Membranes[†]

Roehl M. Cinco,[‡,§] John H. Robblee,[‡,§,||] Johannes Messinger,[§,⊥] Carmen Fernandez,[§,#]
Karen L. McFarlane Holman,[§,△] Kenneth Sauer,[‡,§] and Vittal K. Yachandra*,[§]

Melvin Calvin Laboratory, Physical Biosciences Division, Lawrence Berkeley National Laboratory,
Berkeley, California 94720-5230, and Department of Chemistry, University of California, Berkeley, California 94720-5230

Received December 22, 2003; Revised Manuscript Received July 12, 2004

ABSTRACT: The oxygen-evolving complex of photosystem II (PS II) in green plants and algae contains a cluster of four Mn atoms in the active site, which catalyzes the photoinduced oxidation of water to dioxygen. Along with Mn, calcium and chloride ions are necessary cofactors for proper functioning of the complex. The current study using polarized Sr EXAFS on oriented Sr-reactivated samples shows that Fourier peak II, which fits best to Mn at 3.5 Å rather than lighter atoms (C, N, O, or Cl), is dichroic, with a larger magnitude at 10° (angle between the PS II membrane normal and the X-ray electric field vector) and a smaller magnitude at 80°. Analysis of the dichroism of the Sr EXAFS yields a lower and upper limit of 0° and 23° for the average angle between the Sr−Mn vectors and the membrane normal and an isotropic coordination number (number of Mn neighbors to Sr) of 1 or 2 for these layered PS II samples. The results confirm the contention that Ca (Sr) is proximal to the Mn cluster and lead to refined working models of the heteronuclear Mn_4Ca cluster of the oxygen-evolving complex in PS II.

Calcium is an essential cofactor for photosynthetic oxygen evolution in green plants and algae (*1*−*3*). Without calcium the oxygen-evolving complex (OEC)[1] cannot catalyze the oxidation of water into dioxygen, protons, and electrons. The OEC consists of a tetranuclear manganese cluster (*3*−*5*) that ultimately supplies reducing equivalents to the photooxidized reaction center chlorophyll (P_{680}) through a redox-active tyrosine Y_Z (*6*−*10*). The one-electron photooxidation of P_{680} drives the OEC through a cycle of five intermediates S_i (i = 0−4) (*11*, *12*), where the four oxidizing equivalents are stored before water is finally oxidized into oxygen, four electrons, and four protons. Calcium is needed for the OEC to advance past the S_3 state and subsequent oxygen evolution (*13*, *14*). The involvement and role of manganese in photosynthesis have been extensively studied using biochemical, spectroscopic, and kinetic tools (for reviews see refs *3*, *4*, *7*, and *15*−*18*). X-ray absorption spectroscopy (XAS) (*19*−*23*) and electron paramagnetic resonance (EPR) (*24*−*26*) studies have provided structural and chemical information about the OEC. Because the methods are element-specific and sensitive at dilute concentrations, X-ray absorption near-edge structure (XANES) (*27*−*30*) and extended X-ray absorption fine structure (EXAFS) (*31*−*35*) analyses have been applied at the Mn K-edge to determine oxidation states and provide information about the local environment of the Mn atoms.

In comparison, there have been fewer spectroscopic investigations of the calcium cofactor (*1*, *3*). Most studies on Ca in PS II have been biochemical (*36*−*38*), because Ca has no easy spectroscopic handle, and have shown that depleting Ca by low-pH citrate treatment (*39*) or 1−2 M NaCl wash (*40*, *41*) suppresses oxygen evolution. Replenishing with Ca^{2+} restores catalytic oxygen activity (up to 95%) (*13*, *42*), whereas strontium can reactivate centers to only 40% (*41*, *42*). The smaller rate is due to slower kinetics, because the relative rate is higher (85%) at light-limiting intensity (*14*, *41*). No other metal ion has been shown to restore activity in Ca-depleted centers. This was recently explained by the finding that only Sr matches approximately both the ionic radius of Ca and the pK_a of metal-bound water (*43*). Besides the lower level of recovered oxygen activity (40%), Sr substitution for Ca induces an altered S_2-state EPR multiline signal (MLS) with slightly narrower hyperfine splitting and shifts of the hyperfine lines (*41*, *44*−*46*).

[†] This research was supported by the National Institutes of Health (Grant GM 55302) and by the Director, Office of Science, Office of Basic Energy Sciences, Chemical Sciences, Geosciences, and Biosciences Division of the U.S. Department of Energy (DOE), under Contract DE-AC03-76SF00098. R.M.C. expresses gratitude to the Ford Foundation for a predoctoral fellowship. Additional support was provided by the Fundação de Amparo à Pesquisa do Estado de Sao Paulo (to C.F.) and DFG Grants ME1629/1-1, ME1629/2-1, and ME1629/2-2 (to J.M.).

* To whom correspondence should be addressed. Tel: 510 486 4330. Fax: 510 486 6059. E-mail: vkyachandra@lbl.gov.

[‡] Department of Chemistry, University of California, Berkeley.

[§] Physical Biosciences Division, Lawrence Berkeley National Laboratory.

[||] Present address: Department of Chemistry, Massachusetts Institute of Technology, Cambridge, MA 02139.

[⊥] Present address: Max-Planck-Institut für Bioanorganische Chemie, D-45470 Mülheim an der Ruhr, Germany.

[#] Present address: Departamento de Química Fundamental, Instituto de Química da Universidade de São Paulo, 05508-900 São Paulo, Brazil.

[△] Present address: Department of Chemistry, Willamette University, Salem, OR 97301.

[1] Abbreviations: Chl, chlorophyll; EPR, electron paramagnetic resonance; EXAFS, extended X-ray absorption fine structure; FT, Fourier transform; MLS, multiline EPR signal; OEC, oxygen-evolving complex; PS II, photosystem II; XANES, X-ray absorption near-edge structure; XAS, X-ray absorption spectroscopy.

10.1021/bi036308v CCC: $27.50

The structure of the Ca cofactor binding site has generated considerable discussion. To probe it, the most common approach has been to substitute other metals (such as Sr) for calcium and then use Mn EXAFS (or EPR) to detect changes in the cluster. The first Mn EXAFS study on Sr-reactivated PS II membranes was interpreted to indicate a 3.4−3.5 Å distance between the Sr (and therefore Ca) and the Mn cluster (*35*). This relatively short distance was supported by FTIR spectroscopic evidence using native and Ca-depleted samples that is consistent with a carboxylate bridge between Mn and Ca (*47*, *48*). A slightly longer distance (3.6−3.7 Å) was deduced from a Mn EXAFS study on NaCl-washed PS II membrane preparations (*49*). In contrast, another Mn EXAFS study found no detectable evidence for such an interaction within 4 Å of the Mn, leading to a proposal that Ca was hydrogen-bonded to an oxo bridge between the Mn atoms (*50*). Structural information about the proximity of the Ca cofactor to Mn has been obtained recently through ^{87}Sr ESEEM (electron spin−echo envelope modulation) spectroscopy (R. D. Britt, personal communication). Furthermore, a recent ^{113}Cd NMR study showed that Ca^{2+} is close enough to the Mn_4 cluster to be affected by its spin (*51*).

We have used strontium EXAFS experiments to probe the cofactor itself for any nearby Mn (*52*). This approach differs fundamentally from the previous studies focusing on Mn. By using Sr EXAFS on isotropic Sr-reactivated PS II membranes, we have confirmed the proximity of Sr (and implicitly Ca) at 3.5 Å to the Mn cluster (*52*). The finding was based on the presence of a second Fourier peak in the Sr EXAFS from functional samples, a peak that is absent from inactive, hydroxylamine-treated PS II. This Fourier peak II was found to fit best to Mn rather than lighter atoms (such as C, N, O, or Cl).

In a complementary and definitive experiment, Ca K-edge EXAFS studies have been used to probe the binding site of the native cofactor for any nearby Mn, within ∼4 Å (*53*). The use of Ca EXAFS spectroscopy has produced results essentially congruent with those found by Sr EXAFS on Sr-reactivated PS II. The Fourier transform (FT) of the Ca EXAFS and the spectra are remarkably similar to the FTs of the earlier Sr EXAFS study with Sr substituted for Ca. In contrast to the NH_2OH-treated sample, the Chelex-treated PS II showed a second Fourier peak. When this peak II was isolated and simulated with possible scattering atoms, it corresponded best to Mn at 3.4 Å, rather than to light atom (C, O, or Cl) neighbors.

Conventional EXAFS can provide the absorber−backscatterer distance and the number and identity of scatterers up to 4 Å distance but cannot usually give information about angles or provide geometric information (*54*). However, when applied to oriented samples, such as membrane multilayers, this method can furnish additional angle information. Polarized EXAFS applies linearly polarized synchrotron radiation to partially ordered molecular systems with a preferred orientation along at least one sample coordinate axis (*55*, *56*). Specifically, it has been applied to PS II and other multilayers that possess an effective membrane normal (*31*, *33*, *55*, *57*−*59*). Polarized EXAFS involves collecting spectra for different incident angles (θ) between the membrane normal and the X-ray electric field vector. If dichroism in the EXAFS occurs, it depends on how the particular absorber−backscatterer (A−B) vector is aligned with the electric field. Through analysis of the dichroism, we extract the average orientation (ϕ) of this A−B vector relative to the membrane normal and the average number of scatterers per absorbing atom (N_{iso}). Constraints on the structural model are imposed by these parameters, highlighting the advantage of polarized EXAFS on layered samples over randomly oriented ones.

To date, polarized EXAFS studies on PS II have concentrated on the Mn−Mn vectors (*31*, *33*, *57*−*59*) and have produced valuable insights into the relative angles of the ∼2.7 and ∼3.3 Å Mn−Mn vectors. Previous research on oriented native and NH_3-treated PS II have revealed average angles of ∼60° for the 2.7 Å vectors and ∼43° for the 3.3 Å vectors (*31*, *58*). In contrast, the present study details work using polarized Sr EXAFS on ordered Sr-reactivated PS II membranes. The study shows that Fourier peak II is dichroic: within the range of angles (θ) examined, peak II magnitude is largest at 10° and smallest at 80° (*60*). Analysis of this dichroism leads to the relative orientation of the calcium cofactor involved in oxygen evolution. The results further strengthen the contention that Ca (Sr) is proximal to the Mn cluster and allow us to refine the working model of the oxygen-evolving complex in PS II.

EXPERIMENTAL PROCEDURES

Sample Preparation. PS II-enriched membranes were prepared by Triton X-100 extraction of thylakoids from spinach (*61*). Sr^{2+}-substituted PS II samples were made by a process of Ca depletion by low-pH treatment (*39*, *62*, *63*), Sr^{2+} reactivation (*41*), and Chelex treatment to remove excess Sr (*64*, *65*). These steps have been described in detail previously (*52*) and were carried out in the dark at 4 °C. The samples were assayed for enzyme activity, EPR multiline signal generation (from the S_2 state), and metal quantitation [Mn and Sr from inductively coupled plasma and atomic emission spectroscopy (ICP-AES)]. After the final Chelex treatment to remove nonessential Sr^{2+}, the samples were placed in an SS34 rotor (Sorvall Instruments) and centrifuged (Model RC5B, Sorvall Instruments) for 15 min at 40000*g* in sucrose buffer (0.4 M sucrose, 30 mM NaCl, 50 mM MES, 5 mM $MgCl_2$ and 2.5% ethanol at pH 6.5). The resulting pellet was then painted onto flat Mylar films supported by a Plexiglas frame in dim green light at 4 °C and dried in the dark under a stream of dinitrogen at 4 °C. Six or seven cycles of painting and drying took 12−16 h to build up a sufficient amount of PS II (2−3 mg of Chl) (*31*, *58*). After the last layer had dried, the samples were frozen in liquid nitrogen for storage. Oxygen evolution assays were conducted on samples before the painting process, as mentioned earlier (*52*).

Metal Quantitation. PS II samples (1−3 mg of Chl) were first digested in 3 mL of boiling, concentrated ultrapure HNO_3 (TracePur plus from EM Science or Optima from Fisher Scientific) and then diluted to 10 mL with deionized water. Glass vessels were acid-washed with 10% HCl solution prior to use. Elemental analysis of Mn and Sr in the ppb range was carried out at the Microanalytical Laboratory in the University of California, Berkeley, College of Chemistry using inductively coupled plasma and atomic emission spectroscopy (ICP-AES). The amounts of PS II per sample were calculated from the chlorophyll assays, assuming ~250 Chl per PS II (*66*, *67*).

EPR Spectroscopy. X-band (9.2 GHz) EPR spectra were acquired on layered Sr−PS II on Mylar films, using a Varian E-109 system, a standard TE102 cavity, and a Heli-tran liquid helium cryostat (Air Products). Low-temperature (20 K) spectra were used to monitor EPR-detectable Mn^{2+} in isotropic and layered samples before and after exposure to X-rays. The Ca- and Sr-treated, untreated (native), and layered samples were poised in the S_2 state by illumination for 8 min at 200 K (solid CO_2/ethanol bath) using a 650 W tungsten lamp (General Electric) and an aqueous $CuSO_4$ filter (5% w/v, 7 cm path). Difference (light minus dark) EPR spectra (8 K) were used to characterize the extent of Sr substitution and the turnover of the OEC in pelleted (Sr- and Ca-reactivated) and layered Sr-reactivated samples.

Mosaic Spread Determination by EPR. The paint-and-dry cycles produce one-dimensionally ordered samples with a preferred orientation of the PS II membrane normal perpendicular to the substrate surface. The disorder or mosaic spread (*68*, *69*) can be due to several factors: imperfect stacking of the membranes on the substrate film, disorder of PS II proteins within the membranes, or disorder of the OEC within the PS II proteins. There is no way to assign the contribution of each factor to the total mosaic spread. The extent of orientation can be assessed from the angle dependence of the EPR signal of the cytochrome b_{559} (*31*, *58*, *69*). However, it is cumbersome to collect EPR spectra of cyt b_{559} in several orientations from each sample. We devised a simpler method of correlating the dichroism in the EPR signal from the tyrosine Y_D^{ox} (*24*, *70*, *71*), which is much easier to collect, to that determined from cyt b_{559} (*31*, *58*, *69*, *72*). X-band (9.2 GHz) EPR spectra of the signal II region (near $g = 2.00$) were taken for layered samples oriented 0° and 90° in the magnetic field at 20 K and 50 μW power with 2.5 G modulation amplitude. The sample face was aligned either parallel (0°) or perpendicular (90°) to the external magnetic field. The dichroic ratio (defined here as the amplitude at 90° divided by that at 0°) was taken at ~3260 G. This dichroic ratio ("signal II ratio") was related to the dichroism in the cytochrome b_{559} EPR signal (*24*, *31*, *58*, *69*, *70*, *73*) to obtain the mosaic spread (Ω), or half-width of the Gaussian distribution of a particular vector in PS II samples (*72*). On the basis of previous work from this laboratory (*72*), a calibration line was constructed, equating mosaic spread to a measured signal II ratio. Thus, from the signal II ratio, we can estimate the degree of disorder inherent in the layered samples.

EXAFS Data Collection. Conditions for acquiring Sr EXAFS data on oriented Sr−PS II samples closely resembled those for isotropic samples and have been detailed before (*52*). At the Stanford Synchrotron Radiation Laboratory (SSRL), EXAFS spectra at the Sr K-edge (16−17 keV) were collected on Sr−PS II multilayers at various excitation angles (θ, the angle between the X-ray **e**-field vector and the substrate normal): 10°, 30°, 45°, 70°, and 80° (*31*, *58*). A Si(220) double crystal monochromator was used at the wiggler Beamline VII-3 (unfocused mode) along with a 13-element energy-resolving Ge detector (Canberra Instruments). The X-ray flux at 16−17 keV was between 2 and 5×10^9 photons s^{-1} mm^{-2} of sample (*74*). Samples were kept at a temperature of 10 K in a liquid helium flow cryostat to minimize radiation damage. Six separate samples were used, with at least two angles per sample, for a total of 15 separate data points. Twenty-five to fifty 15 min scans (depending on θ) were necessary for signal averaging to reduce noise to a sufficiently low level. As a check of the sample integrity after Sr substitution and layering treatments, Mn EXAFS data from one sample were also collected for comparison with previously published PS II Mn EXAFS spectra (*35*).

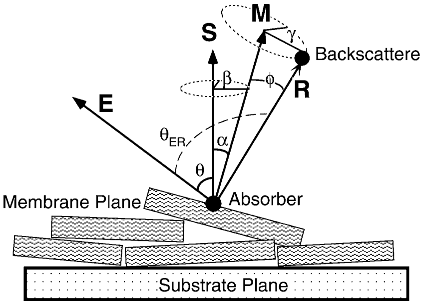

FIGURE 1: Scheme (side view) for the vectors and angles involved in X-ray absorption linear dichroism for partially oriented membranes on a flat surface. Due to rotational symmetry of the layered samples, the orientation of **R** (vector joining the absorber and backscatter defined by the angle ϕ) is described by a cone around the membrane normal **M**. For the polarized EXAFS experiment, spectra are measured for several values of θ (angle between the X-ray electric field vector **E** and the substrate normal **S**), θ_{ER} being the angle between the X-ray electric field vector (**E**) and the absorber−scatterer vector. θ_{ER} is composed of the measurement angle θ and the angle ϕ between **R** and **M**, the membrane normal. Because of the rotational symmetry of the layered membranes, the angle ϕ defines a cone around the membrane normal **M**. When membranes are layered on a flat substrate, the preferential orientation of **M** is parallel to the underlying substrate normal (**S**). For an ensemble of A−B vectors (**R**), the magnitude of the EXAFS is related to the P_α-weighted integration over all possible orientations of **M** (α- and β-integration) and along the cone of possible directions of **R** (γ -integration).

EXAFS Data Analysis. Data reduction has been detailed previously (*52*) and will be only briefly summarized here. After conversion of background-corrected spectra from energy space to photoelectron wave vector (k) space, and weighting by k^3, a five-domain spline was subtracted for a final background removal. The region around $R' = 3.0$ Å, peak II, was isolated using a Hanning window applied to the first and last 15% of the range ($\Delta R = 0.9$ Å), while not affecting the middle 70%. The back-transformed (k-space) peak II was simulated with a Sr−Mn interaction, similar to the isotropic Sr EXAFS protocol (*52*) using ab initio phase and amplitude functions calculated from the program FEFF 7 (*75*−*77*). Curve fitting starting from 3.7 $Å^{-1}$ (so as to conform to the plane-wave approximation in the subsequent analysis of dichroism) was done by minimizing the error sum (Φ) using a nonlinear least-squares protocol while varying these parameters for the Sr−Mn shell: R, N_{app}, and ΔE_0. The Debye−Waller factor (σ^2) was fixed to the best common value (*55*, *57*). For each sample, we compiled a table of the detection angle θ, distance R, apparent coordination number N_{app}, and ΔE_0 (*78*).

Theory of Polarized EXAFS. The dichroism of the Sr−Mn vector (Figure 1) was analyzed using a plane-wave approximation (*78*), and a brief description of the theory is presented here. To analyze the linear dichroism of the Sr EXAFS and find the relative orientation of the vector of interest (ϕ), we used the formalism of Dittmer et al. (*56*, *59*). Although it differs from the previously used protocol of George et al. (*31*, *33*, *55*, *57*, *58*), both methods produce comparable results (within 4−6%). In the plane-wave approximation, the angle dependence of the EXAFS is proportional to $\cos^2\theta$, with θ being the angle between the X-ray electric field vector (**E**) and the absorber−scatterer vector (**R**; see Figure 1) (*56*, *59*). The N_{app} found from EXAFS curve fitting on an oriented sample at a particular θ is related to the coordination number of an isotropic sample N_{iso} by the equation:

$$N_{\mathrm{app}}(\theta) = N_{\mathrm{iso}} + \frac{1}{2}N_{\mathrm{iso}}(3\cos^2\theta - 1)(3\cos^2\phi - 1)I_{\mathrm{ord}} \tag{1}$$

where I_{ord} is the order integral:

$$I_{\mathrm{ord}} = \frac{1}{2}\,\frac{\int_0^{\pi/2}(\sin\alpha)(3\cos^2\alpha - 1)\exp(-\alpha^2\ln 2/\Omega^2)\,\mathrm{d}\alpha}{\int_0^{\pi/2}\sin\alpha\exp(-\alpha^2\ln 2/\Omega^2)\,\mathrm{d}\alpha} \tag{2}$$

By fitting the θ dependence of N_{app} by nonlinear regression analysis, we extract the average relative orientation ϕ and N_{iso}. Equation 1 was implemented numerically by a Mathematica 3.0 program (*79*) (Wolfram Research, Inc.) using values for Ω as determined from EPR. The standard deviations of the parameters ϕ and N_{iso} are more easily obtained from a regression analysis of the linear form of eq 1 (with $x = 3\cos^2\theta - 1$ and $y = N_{\mathrm{app}}$), which was done using Igor Pro software (version 3.1, WaveMetrics Inc.). As a simulated example, Figure S1 (Supporting Information) shows the calculation of eq 1 for various values of the relative angle ϕ, assuming $N_{\mathrm{iso}} = 1$ and $\Omega = 20°$.

RESULTS

The characterizations (EPR, O_2 activity, metal content) yielded results similar to those obtained previously from isotropic samples (*52*). The Sr substitution was judged successful from the Sr-altered EPR S_2-state multiline signal before the Chelex removal of excess Sr, slower steady-state rate of oxygen evolution (40%), and metal content (0.8 Sr per 4 Mn per PS II; the error in Sr quantitation for the six samples is ±0.05). No EPR-detectable Mn^{2+} was observed after the layering process. After the Chelex treatment, comparison of EPR spectra from the oriented and isotropic samples showed that the relative amplitude of the multiline signal was not diminished or adversely affected by the layering process (data not shown). The Mn EXAFS spectra and Fourier transform (Supporting Information, Figure S2) from one oriented sample closely resembled those from native samples and previous Mn EXAFS studies (*31*, *34*, *35*). The EPR and Mn EXAFS spectra together indicated little or no significant damage to the catalytic Mn cluster resulting from the Sr substitution and layering protocols. The EXAFS spectra were all collected using samples in the S_1 state, similar to the previous data that were obtained from isotropic samples.

Mosaic Spread. For simplicity the dichroic ratio of the ∼3260 G feature of the tyrosine Y_D^{ox} (signal II "slow") EPR spectra (*24*, *70*) at two extreme angles (0° and 90°) between the sample face and the applied magnetic field (for details see Figure S3) is used to determine the mosaic spread. This method is based on the previous finding that this ratio is inversely related (*72*) to the mosaic spread as measured from the angle dependence of the cyt b_{559} EPR spectra, following the protocol of Blum et al. (*69*). In addition, we confirmed that with the slightly different method of Dau et al. (*58*) the numbers are practically identical (difference ∼5% in the determination of the coordination numbers). Here, we assumed a Gaussian distribution for the direction of the membrane normal, and the mosaic spread is the half-width of that distribution. In this way, an average mosaic spread of 15 ± 5° was determined for the six samples used in this study.

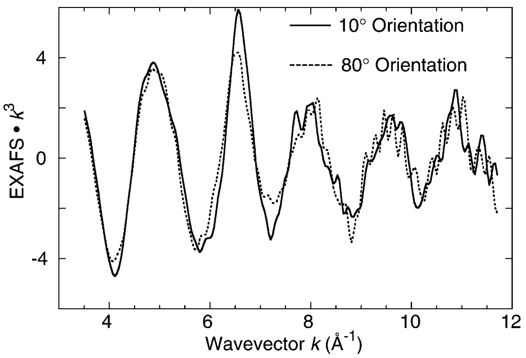

FIGURE 2: k^3-weighted Sr EXAFS of oriented Sr−PS II membranes at two extreme measurement angles ($\theta = 10°$, solid line, and 80°, dashed line). The trace is averaged from five separate samples. The most prominent difference between the two orientations is the damping of the oscillations in the 80° orientation sample in the region of $k = 6-8$ Å^{-1}. The data from each of the individual samples are shown in Figure S4A−F in the Supporting Information.

Polarized Sr EXAFS of Oriented Samples. Figure 2 shows the unfiltered, k^3-weighted Sr EXAFS from the Sr−PS II multilayers at the extreme measurement angles ($\theta = 10°$ and 80°). Data from the various angles (10°, 30°, 45°, 70°, 80°) were processed similarly for consistency and to allow for valid comparisons. The EXAFS data and the Fourier transforms from each of the samples examined are shown in Figure S4A−F (Supporting Information). At each extreme angle, five separate samples were averaged for reproducibility and to achieve high signal-to-noise ratio (Figure 2), with a total of 190 scans at 10° and 160 scans for 80°. Subtle differences between the two orientations were seen, most notably the reduced amplitude oscillations in the region of $k = 6-8$ Å^{-1} for the 80° scans. The differences observed between the two extreme angles are more pronounced in the Fourier transforms.

Fourier Transform (FT) of Polarized Sr EXAFS. The corresponding Fourier transforms (FTs) showed extreme dichroism in peak II for oriented Sr-substituted samples (Figure 3). Among the excitation angles studied, peak II had largest magnitude at $\theta = 10°$, while it is smallest and near the noise level at 80°. For the other experimental angles ($\theta = 30°$ and 45°), the peak II magnitudes (Figure S4A−F, Supporting Information) were intermediate between those at 10° and those at 80°. The dichroism in peak I was undetectable (Figure 3, as measured by relative peak heights at 10° and 80°). Fourier peak I represents the first shell of ligating oxygen atoms and can be simulated by 9 ± 2 oxygens at ∼2.6 Å. The fits are similar to those obtained from earlier studies using isotropic samples and do not

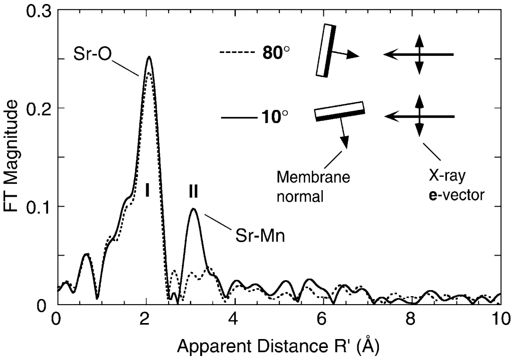

FIGURE 3: Fourier transform of k^3-weighted EXAFS from oriented Sr−PS II samples at two angles (θ). These are the transforms of the corresponding spectra in Figure 2. Each trace is averaged from five separate samples. The dichroism is most readily apparent in Fourier peak II ($R' = 3.0$ Å), where the amplitude is largest at 10° (solid line) and smallest at 80° (dashed line). The inset shows the layered PS II membranes and the underlying substrate in relation to the X-ray **e**-vector, which is perpendicular to the direction of propagation of X-rays. Fourier peak I is backscattering from O and peak II is backscattering from Mn. The data from the individual samples are shown in Figure S4A−F in the Supporting Information.

provide any new insights (*52*). The known coordination numbers of Sr^{2+} range from 6 to 9, and Sr−O distances are distributed from 2.56 to 2.71 Å. Therefore, we concentrate here on the more important longer vector represented by Fourier peak II. The order of data collection (10° then 80° or 80° then 10°) did not affect the pattern of dichroism: the peak II amplitude was always largest at 10°, even after measurement at 80°.

To study the angle dependence of peak II, we performed Fourier isolation of the crucial region ($R' = 2.55-3.45$ Å) from the spectra taken at various angles. For the Fourier isolate at 80°, the EXAFS contribution is much smaller compared to that at 10° as can be expected from the FTs shown in Figure 3, where for the 80° sample the FT peak is within the noise level. The 10° spectra have a large EXAFS contribution and a consistently similar amplitude envelope and were used for curve fitting as described below, whereas the 80° data show much smaller EXAFS contribution and show major differences between two samples. The variation originates from a large component of random noise that is present in the 80° isolates; these isolates cannot be used for EXAFS fitting purposes as these represent mostly noise. The dichroism observed in the FTs (Figures 3 and S4A−F, Supporting Information) is very pronounced and already indicates that the vector of interest is closer to 10° than to 80° from the membrane normal.

EXAFS Curve Fitting. To more precisely determine the angle and distance of this vector, EXAFS curve fitting was applied. The small amplitude of the $\theta = 80°$ isolates made them susceptible to noise and precluded their use in curve fitting. Only other angles (10°, 30°, and 45°) were used in curve fitting. The Fourier isolates at 10°, 30°, and 45° were simulated with one shell of Mn as done previously. Carbon and other light atoms can be ruled out as possible scatterers as previously shown (*52*), and the best fit to 2 Mn is compared to the fit of 6 C (which is the best fit with C) in Figure S5 (Supporting Information). Further shells were unnecessary and produced underdetermined (nonunique) fits. The Debye−Waller factor was fixed to the best value ($\sigma^2 = 0.010$) determined during the fitting procedure, because the static disorder of a Sr−Mn interaction is not expected to show orientation dependence (*55*, *58*).

Table 1: Oriented Sr EXAFS Fitting Results for Peak II ($k = 3.7-11.7$ Å^{-1}) and Corrected N_{app} Values for $\Omega = 15°$ [a]

angle (θ) (deg)	R (Å)	N_{app}	ΔE_0 (eV)	Φ $\times 10^3$	ϵ^2 $\times 10^5$	mosaic spread Ω (deg)	corr N_{app} (at $\Omega = 15°$)
10	3.50	2.9	−1.52	0.415	0.585	18	3.0
10	3.51	3.0	−3.70	0.552	0.748	10	2.8
10	3.51	2.9	−1.75	0.391	0.529	12	2.7
10	3.52	2.8	−0.16	0.392	0.531	11	2.7
10	3.54	2.8	1.69	0.309	0.419	22	2.4
30	3.55	2.2	1.03	0.410	0.633	12	2.0
30	3.46	2.0	−1.80	0.424	0.598	12	1.9
45	3.52	1.4	0.14	0.830	1.222	12	1.4
45	3.50	1.6	1.34	0.332	0.459	11	1.6
70		0.8				22	0.9
80		0.7				18	0.8
80		0.2				10	0.2
80		0.7				12	0.6
80		0.3				12	0.3
80		0.5				11	0.4

[a] The Fourier isolates (data in Supporting Information) taken from each excitation angle were subjected to curve fitting to the EXAFS equation to give the resulting parameters. The value for σ^2 was fixed to the best value for all samples: 0.010. The fit error parameters Φ and ϵ^2 have been discussed before (52). Because the isolates for 70° and 80° were so close to the noise level, their curve fits produced unreliable, suspect values. The N_{app} for 70° and 80° were instead estimated from the relative peak II heights in the Fourier transform, together with the derived N_{app} at 10° (see text for description). The N_{app} corrected to the values expected at $\Omega = 15°$ is described in the text (and using Figure S7). The corrected numbers are plotted in Figure 4.

Table 1 lists the fit results including R, N_{app}, ΔE_0, and the fit error (Φ and ϵ^2), and a representative result of fitting to the 10° spectra is shown in Figure S6 (Supporting Information). The fits are consistent with earlier Sr−Mn fitting results to peak II (*52*): the lower k region ($k = 3.5-4$ Å^{-1}) always has a poorer fit compared to the rest of the k range. For most of the k range (4.5−12 Å^{-1}), the simulation was much better. The deficiency at low k may arise from the simplified situation of using only one Mn shell, because it is possible that lighter atoms can contribute to peak II to a small extent. The limited range of the Fourier isolate ($\Delta R = 1$ Å) precludes the use of more shells of scatterers, which then result in nonunique fits.

Instead of setting $N_{app} = 0$ as has been done in other studies (*33*, *55*), we decided also to estimate the upper limit of N_{app} that could be present in the much reduced peak II based on peak heights in the FTs. The baseline was first measured as the average value of the FT magnitude for R' between 4 and 10 Å (Figure 3), where no real features in R-space are detectable. The dichroic ratio (80°/10°) of peak II was then multiplied by the derived N_{app} at 10° (Table 1) to give an estimate of N_{app} present at 80°. The fractional amount of peak II present at 80° (compared to 10°) was then listed in Table 1 for $\theta = 70°$ and 80°. As a lower limit the FT amplitudes at 70° and 80° were assumed to be zero. The N_{app} values in Table 1 are subject to ±25% systematic error as an inherent limitation of the EXAFS technique (*19*, *80*−*82*).

Determination of ϕ. The values of N_{app} in Table 1 came from six separate samples, each with its own mosaic spread (Ω). Before these values can be combined in a plot of N_{app}

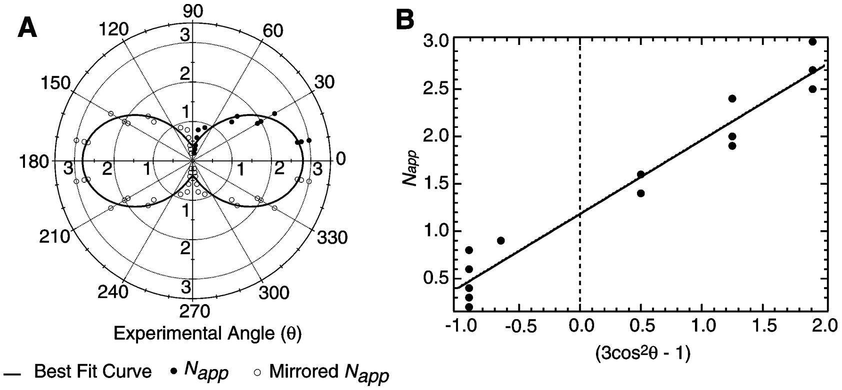

FIGURE 4: (A) Polar plot of the X-ray absorption linear dichroism from oriented Sr−PS II samples. From Table 1, the various corrected N_{app} derived from EXAFS curve fitting are plotted (solid circles) with their respective detection angles (θ). A best fit of N_{app} vs θ is shown as the solid curve (—), according to eq 1 with $\Omega = 15°$. This curve gives $N_{iso} = 1.2$ Mn and $\phi = 23°$. Error bars are discussed in the text. The data points (open circles) and fit between 90° and 360° are mirrored from the $\theta = 0{-}90°$ region. (B) Linear plot of polarized Sr EXAFS data. This form of eq 1 best shows the scatter of the data points in Table 1. From the best-fit slope, ϕ can be calculated (23°) and the intercept yields N_{iso} (1.2). The standard deviations of the slope and intercept are derived from the residuals and translate to random errors in ϕ and N_{iso}.

vs θ, they must be corrected to a common Ω. As stated earlier, the average mosaic spread for the six samples was 15 ± 5°. The correction was made using the plot in Figure S7 (Supporting Information). Equation 1 was simulated for each of three Ω values (10°, 15°, 20°), assuming that $N_{iso} = 1$ and $\phi = 20°$. These are reasonable starting assumptions, based on the observed dichroism in Figure 3 (orientation is likely to be closer to 10° than to 80°). For each measurement angle, the relative correction to N_{app}, when Ω is adjusted to 15°, can be found. For example, at $\theta = 10°$ and sample $\Omega = 10°$, a −5% correction is needed to bring N_{app} in line with $\Omega = 15°$. Likewise, minor adjustments were necessary for the various N_{app} values to allow the use of a common Ω for all 15 points. The original N_{app} values, along with their respective mosaic spread and the corrected N_{app} are listed in Table 1.

With N_{app} found for each excitation angle, θ, we plotted these corrected values in a polar plot shown in Figure 4A and used eq 1 to find the relative orientation (ϕ) of the Sr−Mn vector and its isotropic coordination number N_{iso}. Nonlinear least-squares regression analysis produced the solid curve shown in Figure 4A as the best fit of the 15 data points (angles from six separate samples) to eq 1. Based on the mathematical simulation, the best-fit parameters were $\phi = 23°$ and $N_{iso} = 1.2$. When the N_{app} values for the 70°, 80°, and 90° samples were set to zero or were excluded from the fit, an $N_{iso} = 1.0$ and ϕ value of 0° were obtained (data not shown).

The six distinct samples (sets of two to three incident angles each; data shown in Figure S4A−F) were also analyzed and fit separately. This is beneficial because, for each sample, the data from the different excitation angles share the same mosaic spread and same Sr content. The results for each sample then require no mosaic spread correction. However, the statistics are poorer: 2-, 3-, or 4-point sets compared to a 15-point set. The average of the six sets of extracted parameters ($\phi = 23 \pm 8°$ and $N_{iso} = 1.2$) from the individual samples closely matched the results from the collective (15-point) fit mentioned above. However, when the N_{app} values for the 70°, 80°, and 90° samples were set to zero, a ϕ value of 0° was obtained.

DISCUSSION

Analysis of Error in N_{iso} and ϕ. The major sources of systematic error in the extracted parameters come from the uncertainties in N_{app} and in the mosaic spread. Most of the random error is due to the statistical distribution of the data points or the curve fitting error to eq 1. (We assume that θ is accurately determined, with negligible error.) First, the N derived from EXAFS curve fitting can incur an error of ±25% as described earlier (*19*, *80*, *81*) due to an inherent limitation of the EXAFS technique. This error range was also validated in a recent EXAFS study of distorted Mn cubane complexes, where the N_{Mn-Mn} derived from curve fitting was compared to known crystallographic values (*82*). Therefore, we should allow for ±25% error in the N_{app} listed in Table 1, including those for 70° and 80°, because they were calculated on the basis of the 10° values. The systematic error in N_{app} translates to an error of ±25% in the fit-derived N_{iso} (±0.3).

Second, there was uncertainty in the mosaic spread used for the fitting to eq 1. As stated previously, each of the six samples had an individual mosaic spread value, but in the collective fit, we used the average Ω (15 ± 5°). In doing so, we accounted for the variability in Ω by correcting each N_{app} to the value expected at $\Omega = 15°$. The adjustments allowed us to greatly reduce this type of systematic error.

Third, the evidence for random error is seen in the statistical distribution of data points in the plot in Figure 4. The scatter in the points is best shown in the linear plot of eq 1 in Figure 4B. The best-fit line yields N_{iso} from the N_{app} axis intercept and ϕ from the slope. This is the first time, to our knowledge, that the dichroism eq 1 has been cast in a linear manner as compared to the more traditional polar form shown in Figure 4A. The linear form shown in Figure 4B is an elegant way to obtain N_{iso} and ϕ from the intercept and slope of the best-fit line, respectively, and exhibit the scatter in the data points in a manner that is easy to visualize. However, the least-squares fit of eq 1 to the points in Figure 4B is imperfect; therefore, the derived values of N_{iso} and ϕ incur a standard deviation based on the residuals and the goodness of fit (*79*, *83*). This implicitly assumes that the errors are normally distributed with zero mean and constant variance (*84*). For the best-fit line in Figure 4B, the errors are related to the standard deviations in the slope and the *y*-intercept. From analysis of the residuals in Figure 4B, the resulting standard deviations are ±4° for ϕ and ±0.1 for N_{iso}. As mentioned before, though, the larger systematic error in N_{iso} (±0.3) outweighs the random fitting error (±0.1). After this error analysis, final values for the important parameters are $\phi = 23 \pm 4°$ (the upper limit) and $N_{iso} = 1.2 \pm 0.3$. However, as described in the Results section, the lower limit of 0° for ϕ is obtained when N_{app} for the 70°, 80°, and 90° samples is set to zero or when these points are not included in the fit.

Implications of the Polarized Sr EXAFS Results. Analysis of the pronounced dichroism in the Sr EXAFS (Figures 3, 4, and S4A−F) indicates that the relative orientation (ϕ) of the Sr−Mn vector(s) (0° or 23°) is closer to 10° than 80° and N_{iso} is 1.2 ± 0.3. Referring to Figure 1, the orientation (ϕ) is a cone around the membrane normal, with the Sr−Mn vector (**R** in Figure 1) tilted 23° (upper limit) or 0° (lower limit) from the membrane normal. The observed dichroism and the curve fitting of Fourier peak II further support the previous finding that Mn is within 3.5 Å of the Ca (Sr) cofactor (*52*). If many (∼6) light atoms such as C or O accounted for Fourier peak II (see Figure S5 in Supporting Information), such a marked dichroism would be unlikely, because it would be difficult, but not impossible, to align so many vectors in a parallel or perpendicular orientation with the X-ray **e**-vector to produce the observed behavior.

The presence of at least one Sr (Ca)−Mn vector making an angle (ϕ) between 0° and 23° to the membrane normal is clear from the data presented above. However, determining whether there is one or two or three such Sr (Ca)−Mn interactions (N_{iso}) is more difficult. As the discussion below shows, on the basis of the data from isotropic and oriented samples there maybe two such Sr (Ca)−Mn interactions. Our recent study on anisotropic samples was consistent with two to three interactions (*52*) while the current results yield ∼1.2. Since all of the sample characterization described in the Experimental Procedures indicates that both the oriented and anisotropic samples are intact, we cannot provide a straightforward explanation for this difference. We present factors that could contribute to the differences between the two studies below.

Sample preparation for the two types of samples (isotropic and oriented) is identical up to the point of layering. At this point, while active in oxygen evolution, the isotropic samples are frozen in liquid nitrogen, while the oriented samples undergo a further 8−12 h of paint-and-dry cycles. The EXAFS samples from both preparations are in the S_1 state. The light-induced S_2-state EPR multiline spectra (light minus dark) are essentially identical, indicating no apparent damage to the Mn cluster from the layering process (not shown). We compared the Mn EXAFS from the oriented samples and the isotropic Sr−PS II (see Supporting Information, Figure S2). There are no significant differences to indicate increased damage to the Mn cluster itself or Mn^{2+} release during the drying process. The results were virtually identical to each other and to other Mn EXAFS of Sr-reactivated PS II as prepared previously (*35*).

The difference in coordination number is likely attributable to the extra step of the layering procedure applied to the oriented samples. The above experiments indicate that the Mn_4 cluster is essentially unaltered after drying, but the process could induce changes in the local environment of the Sr cofactor, such as the loss of one or a fraction of the Sr−Mn vectors. The loss of an H_2O bridge [such as one of the two O-bridges depicted in an earlier working model (*52*)] will introduce more disorder or a longer distance (>3.5 Å) into that Sr−Mn vector, rendering it undetectable by EXAFS and leaving *N* closer to unity. Accounting for the difference caused by the drying process, we speculate that there could be two vectors originally, which are indistinguishable with an average angle of 0° or 23° and average distance of 3.5 Å. Figure 5 summarizes the findings of the polarized Sr EXAFS and depicts a simple, reasonable interpretation of the data: two Mn neighbors at the same distance and orientation. However, we emphasize that the present data are consistent with either one or two Sr−Mn vectors.

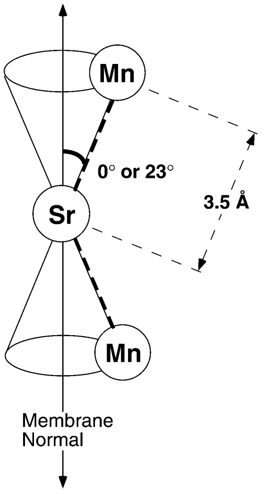

FIGURE 5: Schematic motif summarizing the polarized Sr EXAFS results. The derived coordination number is $N = 1.2 \pm 0.3$, and the average distance is 3.5 Å. Although the figure shows two Sr−Mn interactions, at present the data are consistent with either one or two Sr−Mn vectors at an average orientation, with a lower and upper limit of 0° and 23° to the membrane normal and an average distance of 3.5 Å (see text for explanation). Because of the one-dimensional order in these samples, the up and down directions are equivalent. Bridging oxygen atoms that connect the Sr and Mn atoms have been omitted for clarity.

Working Models of the OEC. The orientation data from the Sr EXAFS experiments can be combined with the published dichroism data from Fourier peak III in the Mn EXAFS from Mukerji et al. (*31*) and Dau et al. (*58*) to calculate the dichroism of the 3.3 Å Mn−Mn vector. As previously described by Mukerji et al. (*31*), Fourier peak III from Mn EXAFS data, which contains equal numbers of Mn−Mn (3.3 Å) and Mn−Ca (3.4 Å) contributions, is dichroic, with an average angle of 43 ± 10° with respect to the membrane normal. Moreover, the 43 ± 10° estimate is a $\cos^2 \phi$-weighted average of the orientations of the Mn−Mn (3.3 Å) and the Mn−Ca vectors (*55*, *57*, *58*) as shown in the equation:

$$\cos \langle\phi\rangle = \sqrt{\sum_{b=1}^{n_b} n_b \cos^2 \phi_{ab} \Big/ \sum_{b=1}^{n_b} n_b} \qquad (3)$$

where the average $\langle\phi\rangle$ can be deconvolved into its n_b number of indistinguishable ϕ_{ab} component vectors. Although Mn−

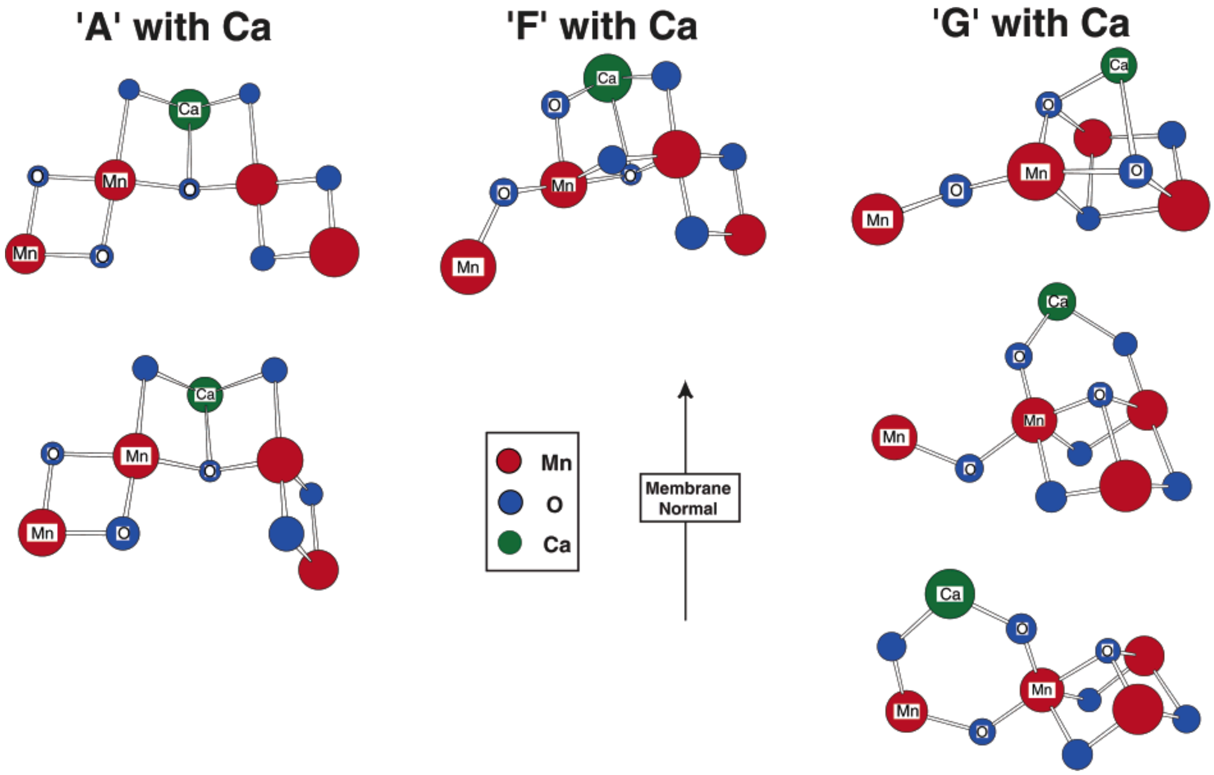

FIGURE 6: Refined models for the active site of the OEC in photosystem II in the S_1 state. These models combine the finding from oriented Sr-substituted PS II samples (Figure 5) with previous results from Mn EXAFS on oriented PS II samples. The models are depicted with two Sr−Mn interactions; however, at present, the data are consistent with either one or two Sr−Mn vectors. These models are derived from core structures that have been described in earlier studies (from options A, F, and G) by DeRose et al. (*34*), Cinco et al. (*82*), and Robblee et al. (*85*).

Mn and Mn−Ca vectors are different, the backscattering properties of Mn and Ca are similar enough that they can be considered indistinguishable ϕ_{ab} component vectors for the calculation of the individual angles.

Our finding from the Sr EXAFS experiments that the Mn−Ca angle is 0° or 23° leads to solutions for the Mn−Mn contribution of 75° or 62° (when we consider two Ca−Mn vectors) and 57° or 52° (when we consider one Ca−Mn vector), respectively, for the 3.3 Å Mn−Mn vector relative to the membrane normal. As mentioned in the introduction, previous polarized Mn EXAFS experiments on PS II have shown angles of 55° and 67° for the 2.7 Å Mn−Mn vectors. Thus the 2.7 and 3.3 Å Mn−Mn vectors then lie at an average angle of 57−65° with respect to the membrane plane but are not restricted to being collinear, because the PS II membranes are ordered in one dimension only. The range of 57−65° is obtained because of the uncertainty in the Mn−Ca angle and in the number of such interactions (one or two); it also depends on whether we include two or three Mn−Mn vectors at ∼2.7 Å in the calculation (*85*). These conclusions can be compared with the recent X-ray crystallography studies of PS II (*86*, *87*). The present structure is of limited resolution, but it is possible to discern a cluster of four atoms attributable to Mn. The arrangement of the Mn atoms has been described as pear-shaped (an elongated ellipsoid) with all four Mn lying approximately in the same plane at an average angle of ∼67° to the membrane normal. The location of Ca relative to this cluster has not yet been reported from X-ray diffraction studies.

Because significant angle information about Mn−Mn and Mn−Ca vectors is now available, other topological models previously discussed (*34*, *82*) can be refined to include the presence of Ca and account for the dichroism data (Figure 6). We have chosen to modify three options [from Figure 9 of DeRose et al. (*34*)]: option A, where the two di-μ-oxo binuclear units are connected by a mono-μ-oxo bridge, option F, where the two di-μ-oxo motifs are formed using a common Mn atom and the mono-μ-oxo motif is placed at the end of the trinuclear unit, and option G, where three Mn atoms can be thought of as at the corners of the base of a trigonal pyramid, with an O atom at the apex and three additional O atoms forming bridges pairwise among the Mn atoms below the base with the fourth Mn linked to one of the corner Mn atoms by a single O-atom bridge. Options A and F both have two 2.7−2.8 Å Mn−Mn vectors while option G has three such vectors. The proposed structures are for the Mn complex in the S_1 state.

One possible modification for option A is the structure shown in the earlier Sr EXAFS study (*52*); however, this arrangement, with the Ca at the “open” end of the complex, places the Ca−Mn and 3.3 Å Mn−Mn vectors roughly parallel, which is inconsistent with the current dichroism data for these vectors. Placing the Ca between the two Mn atoms in the middle of the complex resolves this discrepancy, and the angle between the two di-μ-oxo planes can now be adjusted. Figure 6 shows two possibilities (A with Ca) for this configuration of Mn and Ca atoms. These placements are consistent with the dichroism results from the 2.7 Å Mn−Mn, 3.3 Å Mn−Mn, and 3.4 Å Mn−Sr (Ca) vectors.

Ca can be incorporated into option F [Figure 9 from DeRose et al. (*34*)], which has two di-μ-oxo bridged Mn−Mn moieties adjacent to each other and linked to another

Mn atom via a mono-μ-oxo bridge. Ca forms an open cubane with two Mn atoms forming the other two corners (Figure 6, F with Ca). This arrangement of Ca and Mn atoms is preferred by density functional theory simulations and simulations of EPR and ENDOR data from the OEC (*88*−*90*); a variant of this structure has been proposed by Siegbahn (*88*). Both types of models are variations of a general model proposed earlier (*52*).

Options A and F are both characterized by two 2.7−2.8 Å Mn−Mn vectors and one 3.3 Å Mn−Mn vector. Recent studies on the S_0 state of the OEC have proposed the intriguing possibility that there exist three 2.7−2.8 Å Mn−Mn vectors and one 3.3 Å Mn−Mn vector (*85*). One such topological structure is option G, which was originally suggested among others in an earlier publication from our group [Figure 9 from DeRose et al. (*34*)] and is an example that is also preferred on the basis of EPR and ENDOR data (*89*, *90*). Several geometric isomers of the model are possible, but they all satisfy the basic criteria. Two additional structures, L and M [from Robblee et al. (*85*)], are also modifications of G. We have used G to incorporate Ca in accordance with the Sr and Ca EXAFS data and the orientation of the Sr−Mn vector determined in this study. Three such options are structures are shown in Figure 6 (G with Ca).

In each of the models in Figure 6, the metal atoms are not collinear, thus eliminating focusing effects. If Mn or Ca were collinear with another Mn atom, the focusing from the intermediate atom, presumably an oxygen, would lead to easily discernible intense features in the EXAFS and the FT (*91*, *92*). The lack of any such features in the Mn and Sr EXAFS rules out the presence of such an effect. This is an important criterion for testing possible models of the OEC. F with Ca and G with Ca seem to model best the planarity and Y shape of the Mn atoms in the membrane plane as required by the electron density (*86*, *87*) and EPR and ENDOR results (*88*−*90*).

Recently, we explored the idea that the Mn−Ca cluster in the OEC could be similar to that found in tunnel-like MnO_2, an hypothesis originally put forward by Russell and Hall (*93*) speculating that in PS II the MnO cluster and associated Ca had its evolutionary origin in the capture of Mn oxide precipitates in the early ocean by a non-oxygen-evolving photosynthetic precursor microorganism. We have identified Mn clusters (A, F, and G were all identified in such minerals) with the requisite number of ∼2.7 and ∼3.3 Å Mn−Mn vectors in such MnO_2 minerals (*94*). However, what is most relevant to the present study is that the MnO_2 minerals commonly occur with incorporated Ca or other mono- or divalent cations. These are located between the layers of MnO_2 and exchangeable with ions in an essentially aqueous environment. It is not difficult to imagine a scenario in which a cluster of 4 Mn and 1 Ca with associated oxygen atoms was captured from a medium from which these minerals were precipitating. The Ca location is similar in these Mn minerals to those proposed above (*94*).

In conclusion, we recently improved on previous Mn EXAFS studies by using Sr EXAFS on isotropic samples to confirm the proximity of the Ca (Sr) cofactor to the Mn cluster but could not provide information besides distances. In this study, polarized Sr EXAFS on oriented samples has resulted in angle information about the calcium cofactor to refine the model for the oxygen-evolving complex of PS II. The evidence presented reinforces the concept of a Mn_4Ca heteronuclear cluster as the catalytic center of water oxidation.

NOTE ADDED IN REVISION

We note that a new X-ray crystal structure of photosystem II from *Thermosynechococcus elongatus* at a slightly improved resolution of 3.5 Å has been published (*95*) since this paper was submitted. Electron density from Ca has been identified within the larger volume assigned to the metal cluster by collecting data at energies above and below the Mn K-edge, at 6548 and 5500 eV, respectively. At the present resolution of the X-ray data, the metal to metal and ligand distances cannot be determined with certainty. The proposed structure was hence derived using information from spectroscopic data including the metal to metal and ligand distances derived from XAS studies, and it is very similar to structures discussed in this publication. The structure surely will be refined as higher resolution data are collected. The proposed Mn_4Ca structures, labeled F with Ca and G with Ca in Figure 6 in this paper on the basis of EXAFS data, seem to model best the electron density from the three different X-ray diffraction studies (*86*, *87*, *95*). We are working on simulations of the EXAFS data based on the electron densities, and it will be the subject of a future publication.

ACKNOWLEDGMENT

Synchrotron radiation facilities were provided by the Stanford Synchrotron Radiation Laboratory (SSRL), which is operated by the Department of Energy, Office of Basic Energy Sciences. We thank Dr. Matthew Latimer at SSRL for many useful discussions about fitting polarized EXAFS data. The SSRL Biotechnology Program is supported by the National Institutes of Health, National Center of Research Resources, Biomedical Technology Program, and by the Department of Energy, Office of Health and Environmental Research.

SUPPORTING INFORMATION AVAILABLE

Simulated polar plots of EXAFS amplitudes, control Mn EXAFS data from Sr-reconstituted isotropic and oriented PS II samples, EXAFS data and Fourier transforms from all the samples, best fits to Sr EXAFS from Sr-reconstituted samples, and dependence of N_{app} with mosaic spread. This material is available free of charge via the Internet at http://pubs.acs.org.

REFERENCES

1. Yocum, C. F. (1991) Calcium activation of photosynthetic water oxidation, *Biochim. Biophys. Acta 1059*, 1−15.
2. Boussac, A., and Rutherford, A. W. (1994) The oxygen-evolving enzyme: Effects of calcium and chloride ions, *Biochem. Soc. Trans. 22*, 352−358.
3. Debus, R. J. (1992) The manganese and calcium ions of photosynthetic oxygen evolution, *Biochim. Biophys. Acta 1102*, 269−352.
4. Yachandra, V. K., Sauer, K., and Klein, M. P. (1996) Manganese cluster in photosynthesis: Where plants oxidize water to dioxygen, *Chem. Rev. 96*, 2927−2950.
5. Renger, G. (1997) Mechanistic and structural aspects of photosynthetic water oxidation, *Physiol. Plant. 100*, 828−841.

6. Diner, B. A., and Babcock, G. T. (1996) in *Oxygenic photosynthesis: The light reactions* (Ort, D. R., and Yocum, C. F., Eds.) pp 213−247, Kluwer Academic Publishers, Dordrecht.
7. Britt, R. D. (1996) in *Oxygenic photosynthesis: The light reactions* (Ort, D. R., and Yocum, C. F., Eds.) pp 137−164, Kluwer Academic Publishers, Dordrecht.
8. Babcock, G. T., Espe, M., Hoganson, C. W., Lydakis-Simantiris, N., McCracken, J., Shi, W., Styring, S., Tommos, C., and Warncke, K. (1997) Tyrosyl radicals in enzyme catalysis: Some properties and a focus on photosynthetic water oxidation, *Acta Chem. Scand. 51*, 533−540.
9. Hoganson, C. W., and Babcock, G. T. (1997) A metalloradical mechanism for the generation of oxygen from water in photosynthesis, *Science 277*, 1953−1956.
10. Tommos, C., and Babcock, G. T. (1998) Oxygen production in nature: A light-driven metalloradical enzyme process, *Acc. Chem. Res. 31*, 18−25.
11. Joliot, P., and Kok, B. (1975) Oxygen evolution in photosynthesis, in *Bioenergetics of photosynthesis* (Govindjee, Ed.) pp 387−412, Academic Press, New York.
12. Kok, B., Forbush, B., and McGloin, M. (1970) Cooperation of charges in photosynthetic O_2 evolution, *Photochem. Photobiol. 11*, 457−476.
13. Boussac, A., Maison-Peteri, B., Etienne, A.-L., and Vernotte, C. (1985) Reactivation of oxygen evolution of NaCl-washed photosystem II particles by Ca^{2+} and/or the 24 kDa protein, *Biochim. Biophys. Acta 808*, 231−234.
14. Boussac, A., and Rutherford, A. W. (1988) S-state formation after Ca^{2+} depletion in the photosystem II oxygen-evolving complex, *Chem. Scr. 28A*, 123−126.
15. Rutherford, A. W., Zimmermann, J.-L., and Boussac, A. (1992) Oxygen evolution, in *The photosystems: Structure, function, and molecular biology* (Barber, J., Ed.) pp 179−229, Elsevier B. V., Amsterdam.
16. Yachandra, V. K., DeRose, V. J., Latimer, M. J., Mukerji, I., Sauer, K., and Klein, M. P. (1993) Where plants make oxygen: A structural model for the photosynthetic oxygen-evolving manganese cluster, *Science 260*, 675−679.
17. Yocum, C. F., and Pecoraro, V. L. (1999) Recent advances in the understanding of the biological chemistry of manganese, *Curr. Opin. Chem. Biol. 3*, 182−187.
18. Messinger, J. (2000) Towards understanding the chemistry of photosynthetic oxygen evolution: Dynamic structural changes, redox states and substrate water binding of the Mn cluster in photosystem II, *Biochim. Biophys. Acta 1459*, 481−488.
19. Cramer, S. P. (1988) Biochemical applications of X-ray absorption spectroscopy, in *X-ray absorption: Principles, applications and techniques of EXAFS, SEXAFS, and XANES* (Koningsberger, D. C., and Prins, R., Eds.) pp 257−320, Wiley-Interscience, New York.
20. Yachandra, V. K. (1995) X-ray absorption spectroscopy and applications in structural biology, *Methods Enzymol. 246*, 638−675.
21. Yachandra, V. K., and Klein, M. P. (1996) X-ray absorption spectroscopy: Determination of transition metal site structures in photosynthesis, in *Biophysical techniques in photosynthesis* (Amesz, J., and Hoff, A. J., Eds.) pp 337−354, Kluwer Academic Publishers, Dordrecht, The Netherlands.
22. Penner-Hahn, J. E. (1998) Structural characterization of the Mn site in the photosynthetic oxygen-evolving complex, *Struct. Bonding 90*, 1−36.
23. Robblee, J. H., Cinco, R. M., and Yachandra, V. K. (2001) X-ray spectroscopy-based structure of the Mn cluster and mechanism of photosynthetic oxygen evolution, *Biochim. Biophys. Acta 1503*, 7−23.
24. Miller, A.-F., and Brudvig, G. W. (1991) A guide to electron paramagnetic resonance spectroscopy of photosystem II membranes, *Biochim. Biophys. Acta 1056*, 1−18.
25. Britt, R. D., Peloquin, J. M., and Campbell, K. A. (2000) Pulsed and parallel-polarization EPR characterization of the photosystem II oxygen-evolving complex, *Annu. Rev. Biophys. Biomol. Struct. 29*, 463−495.
26. Peloquin, J. M., and Britt, R. D. (2001) EPR/ENDOR characterization of the physical and electronic structure of the OEC Mn cluster, *Biochim. Biophys. Acta 1503*, 96−111.
27. Roelofs, T. A., Liang, W., Latimer, M. J., Cinco, R. M., Rompel, A., Andrews, J. C., Sauer, K., Yachandra, V. K., and Klein, M. P. (1996) Oxidation states of the manganese cluster during the flash-induced S-state cycle of the photosynthetic oxygen-evolving complex, *Proc. Natl. Acad. Sci. U.S.A. 93*, 3335−3340.
28. Ono, T.-A., Noguchi, T., Inoue, Y., Kusunoki, M., Matsushita, T., and Oyanagi, H. (1992) X-ray-detection of the period-4 cycling of the manganese cluster in the photosynthetic water oxidizing enzyme, *Science 258*, 1335−1337.
29. Iuzzolino, L., Dittmer, J., Dörner, W., Meyer-Klaucke, W., and Dau, H. (1998) X-ray absorption spectroscopy on layered photosystem II membrane particles suggests manganese-centered oxidation of the oxygen-evolving complex for the S_0−S_1, S_1−S_2, and S_2−S_3 transitions of the water oxidation cycle, *Biochemistry 37*, 17112−17119.
30. Messinger, J., Robblee, J. H., Bergmann, U., Fernandez, C., Glatzel, P., Visser, H., Cinco, R. M., McFarlane, K. L., Bellacchio, E., Pizarro, S. A., Cramer, S. P., Sauer, K., Klein, M. P., and Yachandra, V. K. (2001) Absence of Mn-centered oxidation in the $S_2 \rightarrow S_3$ transition: Implications for the mechanism of photosynthetic water oxidation, *J. Am. Chem. Soc. 123*, 7804−7820.
31. Mukerji, I., Andrews, J. C., DeRose, V. J., Latimer, M. J., Yachandra, V. K., Sauer, K., and Klein, M. P. (1994) Orientation of the oxygen-evolving manganese complex in a photosystem II membrane preparation: An X-ray absorption spectroscopy study, *Biochemistry 33*, 9712−9721.
32. Riggs, P. J., Mei, R., Yocum, C. F., and Penner-Hahn, J. E. (1992) Reduced derivatives of the manganese cluster in the photosynthetic oxygen-evolving complex, *J. Am. Chem. Soc. 114*, 10650−10651.
33. George, G. N., Prince, R. C., and Cramer, S. P. (1989) The manganese site of the photosynthetic water-splitting enzyme, *Science 243*, 789−791.
34. DeRose, V. J., Mukerji, I., Latimer, M. J., Yachandra, V. K., Sauer, K., and Klein, M. P. (1994) Comparison of the manganese oxygen-evolving complex in photosystem II of spinach and *Synechococcus* sp. with multinuclear manganese model compounds by X-ray absorption spectroscopy, *J. Am. Chem. Soc. 116*, 5239−5249.
35. Latimer, M. J., DeRose, V. J., Mukerji, I., Yachandra, V. K., Sauer, K., and Klein, M. P. (1995) Evidence for the proximity of calcium to the manganese cluster of photosystem II: Determination by X-ray absorption spectroscopy, *Biochemistry 34*, 10898−10909.
36. Chen, C., Kazimir, J., and Cheniae, G. M. (1995) Calcium modulates the photoassembly of photosystem II $(Mn)_4$-clusters by preventing ligation of nonfunctional high-valency states of manganese, *Biochemistry 34*, 13511−13526.
37. Ananyev, G. M., and Dismukes, G. C. (1997) Calcium induces binding and formation of a spin-coupled dimanganese (II, II) center in the apo-water oxidation complex of photosystem II as precursor to the functional tetra-Mn/Ca cluster, *Biochemistry 36*, 11342−11350.
38. Grove, G. N., and Brudvig, G. W. (1998) Calcium binding studies of photosystem II using a calcium-selective electrode, *Biochemistry 37*, 1532−1539.
39. Ono, T.-A., and Inoue, Y. (1988) Discrete extraction of the Ca atom functional for O_2 evolution in higher plant photosystem II by a simple low pH treatment, *FEBS Lett. 227*, 147−152.
40. Boussac, A., Maison-Peteri, B., Vernotte, C., and Etienne, A.-L. (1985) The charge accumulation mechanism in NaCl-washed and in Ca^{2+}-reactivated photosystem II particles, *Biochim. Biophys. Acta 808*, 225−230.
41. Boussac, A., and Rutherford, A. W. (1988) Nature of the inhibition of the oxygen-evolving enzyme of photosystem II induced by NaCl washing and reversed by the addition of Ca^{2+} or Sr^{2+}, *Biochemistry 27*, 3476−3483.
42. Ghanotakis, D. F., Babcock, G. T., and Yocum, C. F. (1984) Calcium reconstitutes high rates of oxygen evolution in polypeptide-depleted photosystem II preparations, *FEBS Lett. 167*, 127−130.
43. Vrettos, J. S., Stone, D. A., and Brudvig, G. W. (2001) Quantifying the ion selectivity of the Ca^{2+} site in photosystem II: Evidence for direct involvement of Ca^{2+} in O_2 formation, *Biochemistry 40*, 7937−7945.
44. Boussac, A., Zimmermann, J.-L., and Rutherford, A. W. (1989) EPR signals from modified charge accumulation states of the oxygen evolving enzyme in Ca^{2+}-deficient photosystem II, *Biochemistry 28*, 8984−8989.
45. Sivaraja, M., Tso, J., and Dismukes, G. C. (1989) A calcium-specific site influences the structure and activity of the manganese cluster responsible for photosynthetic water oxidation, *Biochemistry 28*, 9459−9464.

46. Tso, J., Sivaraja, M., and Dismukes, G. C. (1991) Calcium limits substrate accessibility or reactivity at the manganese cluster in photosynthetic water oxidation, *Biochemistry 30*, 4734−4739.
47. Noguchi, T., Ono, T.-A., and Inoue, Y. (1995) Direct detection of a carboxylate bridge between Mn and Ca^{2+} in the photosynthetic oxygen-evolving center by means of Fourier transform infrared spectroscopy, *Biochim. Biophys. Acta 1228*, 189−200.
48. Noguchi, T., Ono, T.-A., and Inoue, Y. (1995) A carboxylate ligand interacting with water in the oxygen-evolving center of photosystem II as revealed by Fourier transform infrared spectroscopy, *Biochim. Biophys. Acta 1232*, 59−66.
49. MacLachlan, D. J., Hallahan, B. J., Ruffle, S. V., Nugent, J. H. A., Evans, M. C. W., Strange, R. W., and Hasnain, S. S. (1992) An EXAFS study of the manganese O_2-evolving complex in purified photosystem II membrane fractions, *Biochem. J. 285*, 569−576.
50. Riggs-Gelasco, P. J., Mei, R., Ghanotakis, D. F., Yocum, C. F., and Penner-Hahn, J. E. (1996) X-ray absorption spectroscopy of calcium-substituted derivatives of the oxygen-evolving complex of photosystem II, *J. Am. Chem. Soc. 118*, 2400−2410.
51. Matysik, J., Alia, G. N., van Gorkom, H. J., Hoff, A. J., and de Groot, H. J. M. (2000) Exploring the calcium-binding site in photosystem II membranes by solid-state ^{113}Cd NMR, *Biochemistry 39*, 6751−6755.
52. Cinco, R. M., Robblee, J. H., Rompel, A., Fernandez, C., Yachandra, V. K., Sauer, K., and Klein, M. P. (1998) Strontium EXAFS reveals the proximity of calcium to the manganese cluster of oxygen-evolving photosystem II, *J. Phys. Chem. B 102*, 8248−8256.
53. Cinco, R. M., Holman, K. L. M., Robblee, J. H., Yano, J., Pizarro, S. A., Bellacchio, E., Sauer, K., and Yachandra, V. K. (2002) Calcium EXAFS establishes the Mn−Ca cluster in the oxygen-evolving complex of photosystem II, *Biochemistry 41*, 12928−12933.
54. Teo, B. K. (1986) *EXAFS: Basic principles and data analysis*, Springer-Verlag, Berlin.
55. George, G. N., Cramer, S. P., Frey, T. G., and Prince, R. C. (1993) X-ray absorption spectroscopy of oriented cytochrome oxidase, *Biochim. Biophys. Acta 1142*, 240−252.
56. Dittmer, J., and Dau, H. (1998) Theory of the linear dichroism in the extended X-ray absorption fine structure (EXAFS) of partially vectorially ordered systems, *J. Phys. Chem. B 102*, 8196−8200.
57. George, G. N., Prince, R. C., Frey, T. G., and Cramer, S. P. (1989) Oriented X-ray absorption spectroscopy of membrane bound metalloproteins, *Physica B 158*, 81−83.
58. Dau, H., Andrews, J. C., Roelofs, T. A., Latimer, M. J., Liang, W., Yachandra, V. K., Sauer, K., and Klein, M. P. (1995) Structural consequences of ammonia binding to the manganese cluster of the photosynthetic oxygen-evolving complex: An X-ray absorption study of isotropic and oriented photosystem II particles, *Biochemistry 34*, 5274−5287.
59. Schiller, H., Dittmer, J., Iuzzolino, L., Dörner, W., Meyer-Klaucke, W., Solé, V. A., Nolting, H.-F., and Dau, H. (1998) Structure and orientation of the oxygen-evolving manganese complex of green algae and higher plants investigated by X-ray absorption linear dichroism spectroscopy on oriented photosystem II membrane particles, *Biochemistry 37*, 7340−7350.
60. Cinco, R. M., Robblee, J. H., Rompel, A., Fernandez, C., Yachandra, V. K., Sauer, K., and Klein, M. P. (1999) Proximity of calcium to the manganese cluster of the photosynthetic oxygen-evolving complex determined from strontium XAFS, *J. Synchrotron Radiat. 6*, 419−420.
61. Berthold, D. A., Babcock, G. T., and Yocum, C. F. (1981) A highly resolved, oxygen-evolving photosystem II preparation from spinach thylakoid membranes, *FEBS Lett. 134*, 231−234.
62. Ono, T.-A., Izawa, S., and Inoue, Y. (1992) Structural and functional modulation of the manganese cluster in Ca^{2+}-depleted photosystem II induced by binding of the 24-kilodalton extrinsic protein, *Biochemistry 31*, 7648−7655.
63. Kodera, Y., Hara, H., Astashkin, A. V., Kawamori, A., and Ono, T.-A. (1995) EPR study of trapped tyrosine z^+ in Ca-depleted photosystem II, *Biochim. Biophys. Acta 1232*, 43−51.
64. Kashino, Y., Satoh, K., and Katoh, S. (1986) A simple procedure to determine Ca^{2+} in oxygen-evolving preparations from *Synechococcus sp., FEBS Lett. 205*, 150−154.
65. Katoh, S., Satoh, K., Ohno, T., Chen, J.-R., and Kashino, Y. (1987) Numbers of calcium ions associated with oxygen evolving photosystem II preparations with different affinities, in *Progress in photosynthesis research* (Biggins, J., Ed.) pp I.5.625−628, Martinus Nijhoff Publishers, Dordrecht.
66. Han, K.-C., and Katoh, S. (1993) Different localization of two Ca^{2+} in spinach oxygen-evolving photosystem II membranes. Evidence for involvement of only one Ca^{2+} in oxygen evolution, *Plant Cell Physiol. 34*, 585−593.
67. Patzlaff, J. S., and Barry, B. A. (1996) Pigment quantitation and analysis by HPLC reverse phase chromatography: A characterization of antenna size in oxygen-evolving photosystem II preparations from cyanobacteria and plants, *Biochemistry 35*, 7802−7811.
68. Blum, H., Harmon, H. J., Leigh, J. S., Salerno, J. C., and Chance, B. (1978) The orientation of a heme of cytochrome *c* oxidase in submitochondrial particles, *Biochim. Biophys. Acta 502*, 1−10.
69. Blum, H., Salerno, J. C., and Leigh, J. S., Jr. (1978) A model for the simulation of EPR spectra of chromophores in partially oriented membrane multilayers, *J. Magn. Reson. 30*, 385−391.
70. Rutherford, A. W. (1985) Orientation of EPR signals arising from components in photosystem II membranes, *Biochim. Biophys. Acta 807*, 189−201.
71. Lakshmi, K. V., Eaton, S. S., Eaton, G. R., and Brudvig, G. W. (1999) Orientation of the tetranuclear manganese cluster and tyrosine z in the O_2-evolving complex of photosystem II: An EPR study of the $S_2Y_z^{\bullet}$ state in oriented acetate-inhibited photosystem II membranes, *Biochemistry 38*, 12758−12767.
72. Andrews, J. C. (1995) X-ray absorption spectroscopy and EPR studies of oriented spinach thylakoid preparations, Ph.D. Dissertation, Department of Chemistry, University of California, Berkeley, CA, LBNL Report 37695.
73. Hasegawa, K., Kusunoki, M., Inoue, Y., and Ono, T.-A. (1998) Simulation of S_2-state multiline EPR signal in oriented photosystem II membranes: Structural implications for the manganese cluster in an oxygen-evolving complex, *Biochemistry 37*, 9457−9465.
74. Thompson, A. C., and Vaughan, D. (2001), X-ray Data Booklet, Lawrence Berkeley National Laboratory, Berkeley, CA, LBNL/Pub-490 Rev. 2.
75. Rehr, J. J., Mustre de Leon, J., Zabinsky, S. I., and Albers, R. C. (1991) Theoretical X-ray absorption fine structure standards, *J. Am. Chem. Soc. 113*, 5135−5140.
76. Rehr, J. J., Albers, R. C., and Zabinsky, S. I. (1992) High-order multiple scattering calculations of X-ray-absorption fine structure, *Phys. Rev. Lett. 69*, 3397−3400.
77. Zabinsky, S. I., Rehr, J. J., Ankudinov, A., Albers, R. C., and Eller, M. J. (1995) Multiple-scattering calculations of X-ray absorption spectra, *Phys. Rev. B 52*, 2995−3009.
78. Pickering, I. J., and George, G. N. (1995) Polarized X-ray absorption spectroscopy of cupric chloride dihydrate, *Inorg. Chem. 34*, 3142−3152.
79. Wolfram, S. (1996) *The mathematica book*, 3rd ed., Wolfram Media/Cambridge University Press, New York.
80. Bertagnolli, H., and Ertel, T. S. (1994) X-ray absorption spectroscopy of amorphous solids, liquids, and catalytic and biochemical systems-capabilities and limitations, *Angew. Chem., Int. Ed. Engl. 33*, 45−66.
81. Riggs-Gelasco, P. J., Stemmler, T. L., and Penner-Hahn, J. E. (1995) XAFS of dinuclear metal sites in proteins and model compounds, *Coord. Chem. Rev. 144*, 245−286.
82. Cinco, R. M., Rompel, A., Visser, H., Aromí, G., Christou, G., Sauer, K., Klein, M. P., and Yachandra, V. K. (1999) Comparison of the manganese cluster in oxygen-evolving photosystem II with distorted cubane manganese compounds through X-ray absorption spectroscopy, *Inorg. Chem. 38*, 5988−5998.
83. Hecht, H. G. (1990) *Mathematics in chemistry: An introduction to modern methods*, Prentice-Hall, Englewood Cliffs, NJ.
84. WaveMetrics Inc. (1998) *Igor pro user's guide*, Vol. II, WaveMetrics, Lake Oswego, OR.
85. Robblee, J. H., Messinger, J., Cinco, R. M., McFarlane, K. L., Fernandez, C., Pizarro, S. A., Sauer, K., and Yachandra, V. K. (2002) The Mn cluster in the S_0 state of the oxygen-evolving complex of photosystem II studied by EXAFS spectroscopy: Are there three di-μ-oxo-bridged Mn_2 moieties in the tetranuclear Mn complex? *J. Am. Chem. Soc. 124*, 7459−7471.
86. Zouni, A., Witt, H. T., Kern, J., Fromme, P., Krauss, N., Saenger, W., and Orth, P. (2001) Crystal structure of photosystem II from *Synechococcus elongatus* at 3.8 angstrom resolution, *Nature 409*, 739−743.

87. Kamiya, N., and Shen, J. R. (2003) Crystal structure of oxygen-evolving photosystem II from *Thermosynechococcus vulcanus* at 3.7-angstrom resolution, *Proc. Natl. Acad. Sci. U.S.A. 100*, 98−103.
88. Siegbahn, P. E. M. (2000) Theoretical models for the oxygen radical mechanism of water oxidation and of the water oxidizing complex of photosystem II, *Inorg. Chem. 39*, 2923−2935.
89. Hasegawa, K., Ono, T.-A., Inoue, Y., and Kusunoki, M. (1999) Spin-exchange interactions in the S_2-state manganese tetramer in photosynthetic oxygen-evolving complex deduced from $g = 2$ multiline EPR signal, *Chem. Phys. Lett. 300*, 9−19.
90. Peloquin, J. M., Campbell, K. A., Randall, D. W., Evanchik, M. A., Pecoraro, V. L., Armstrong, W. H., and Britt, R. D. (2000) ^{55}Mn ENDOR of the S_2-state multiline EPR signal of photosystem II: Implications on the structure of the tetranuclear cluster, *J. Am. Chem. Soc. 122*, 10926−10942.
91. Westre, T. E., Di Cicco, A., Filipponi, A., Natoli, C. R., Hedman, B., Solomon, E. I., and Hodgson, K. O. (1995) GNXAS, a multiple-scattering approach to EXAFS analysis: Methodology and applications to iron complexes, *J. Am. Chem. Soc. 117*, 1566−1583.
92. Laplaza, C. E., Johnson, M. J. A., Peters, J. C., Odom, A. L., Kim, E., Cummins, C. C., George, G. N., and Pickering, I. J. (1996) Dinitrogen cleavage by three-coordinate molybdenum (III) complexes: Mechanistic and structural data, *J. Am. Chem. Soc. 118*, 8623−8638.
93. Russell, M. J., and Hall, A. J. (2001) The onset of life and the dawn of oxygenic photosynthesis: Respective roles of $[Fe_4S_4]^{2+}$ cubane and transient $[Mn_4O_6]^{6+}$ in CO_2 reduction, in *Sixth international congress on carbon dioxide utilization*, p 49, Breckinridge, CO.
94. Sauer, K., and Yachandra, V. K. (2002) A possible evolutionary origin for the Mn_4 cluster of the photosynthetic water oxidation complex from natural MnO_2 precipitates in the early ocean, *Proc. Natl. Acad. Sci. U.S.A. 99*, 8631−8636.
95. Ferreira, K. N., Iverson, T. M., Maghlaoui K., Barber, J., and Iwata, S. (2004) Architecture of the photosynthetic oxygen-evolving center, *Science 303*, 1831−1838.

BI036308V